A Journal of the Gesellschaft Deutscher Chemiker

Angewandte International Edition Chemie

GDCh

www.angewandte.org

## Accepted Article

**Title:** Linkage Microenvironment of Azoles-Related Covalent Organic Frameworks Precisely Regulates Photocatalytic Generation of Hydrogen Peroxide

**Authors:** Yi Mou, Xiaodong Wu, Chencheng Qin, Junying Chen, Yanlan Zhao, Longbo Jiang, Chen Zhang, Xingzhong Yuan, Edison Huixiang Ang, and Hou Wang



**To be cited as:** *Angew. Chem. Int. Ed.* **2023**, e202309480

**Link to VoR:** https://doi.org/10.1002/anie.202309480

WILEY VCH

10.1002/anie.202309480

WILEY-VCH

RESEARCH ARTICLE

# Linkage Microenvironment of Azoles-Related Covalent Organic Frameworks Precisely Regulates Photocatalytic Generation of Hydrogen Peroxide

Yi Mou[+,a], Xiaodong Wu[+,b], Chencheng Qin[a], Junying Chen[a], Yanlan Zhao[a], Longbo Jiang[a], Chen Zhang[a], Xingzhong Yuan[a], Edison Huixiang Ang[c], Hou Wang *[a]

[a] [+]Y. Mou, C. C. Qin, Y.J. Chen, Prof. L.B. Jiang, Prof. C. Zhang, Prof. X. Y. Yuan, Prof. H. Wang
College of Environmental Science and Engineering, Key Laboratory of Environmental Biology and Pollution Control
Hunan University
Changsha 410082, P. R. China
E-mail: wangh@hnu.edu.cn (H. Wang)
[b] [+]Prof. X. Wu
College of Materials Science and Engineering
Nanjing Tech University
Nanjing 210009, P. R. China
[c] Prof. E. H. Ang
Natural Sciences and Science Education,
National Institute of Education, Nanyang Technological University
Singapore 637616, Singapore.
[+] These authors contributed equally to this work.

**Abstract:** Artificial $H_2O_2$ photosynthesis by covalent organic frameworks (COFs) photocatalysts is promising for wastewater treatment. The effect of linkage chemistry of COFs as functional basis to photoelectrochemical properties and photocatalysis remains a significant challenge. In this study, three kinds of azoles-linked COFs including thiazole-linked TZ-COF, oxazole-linked OZ-COF and imidazole-linked IZ-COF were successfully synthesized. More accessible channels of charge transfer were constructed in TZ-COF via the donor-π-acceptor structure between thiazole linkage and pyrene linker, leading to efficient suppression of photoexcited charge recombination. Density functional theory calculations support the experimental studies, demonstrating that the thiazole linkage is more favorable for the formation of $*O_2$ intermediate in $H_2O_2$ production than that of the oxazole and imidazole linkages. The real active sites in COFs located at the benzene ring fragment between pyrene unit and azole linkage.

## Introduction

Covalent organic frameworks (COFs), consisting of linkers and linkages, has advanced significantly in recent years as their distinct physicochemical characteristics, for instance, rationale design structure, customizable functions, simple structural modification, and so on[1]. It is possible to adjust some characters through crystallinity, linker species, linkage chemistry, and many other factors[2]. Imine-based COFs, has received a lot of attention, and combines relatively simple crystallization with controllable composition and porosity. However, it has inherent limitations that imine linkages are less stable in harsh chemical environments and in-plane π-conjugation is inappropriate due to inherent polarization of imine bond[3].

A substitution of linkages obtained from chemically transformed and locked imine bonds offers promising perspective to address this issue. Among these, azole linkages have been shown to be effective in enhancing chemical stability and π-conjugation[4]. In photocatalytic conversion of 4-carboxyphenylboronic acid into 4-hydroxybenzoic acid, for instance, the oxazole-linked LZU-190 stands out, whereas imine-linked COF-LZU1 disintegrates[5]. Thiazole-linked BTZ-TPA-COF possessed good photocatalytic conversion of phenylboronic acid to phenol[6]. In compared with imine-linked COFs, the heterocyclic structure of linkage in COFs is prone to endow lower band gap through conjugation or donor-acceptor interactions[7]. And azoles linkage in COFs improved the degree of π conjugation for further enhancing photocatalytic performance[8]. However, there exists great gap between pyrrole-like heteroatoms of linkage in reticular chemistry and photocatalytic performance, which has not yet been reported.

The design of "donor-π-acceptor" (D-π-A) structure is one of the most traditional and useful manner toward creating exceptional semiconductors by influencing the photon-capture efficiency, and the splitting of photogenerated excitons[9]. Azole linkages were more frequently employed as acceptor units due to the electron-deficient characteristics of pyridine N[10]. Pyrene was explored as a donor unit due to its highly symmetrical tetraphenyl ring structure, big π-conjugation system, and strong photoactivity [11]. Thus, the whole D-π-A structure was created, and the linker between pyrrole-like atomic changes and performance differences was precisely achieved. Furthermore, there is a distinct ordering of electronegativity between the three, O>N>S [12], which may cause the frame characteristics to follow this pattern.

Artificial hydrogen peroxide ($H_2O_2$) photosynthesis is promising technology to restore the water environment as an environmentally friendly strong oxidant. It avoided the risk of explosion of traditional anthraquinone methods and reduces transport costs[13]. $H_2O_2$ photosynthesis can be chosen as a model reaction to investigate the relationships between linkage chemistry and photocatalytic performance. It consists of two half-reactions: oxygen reduction reaction (ORR) and water oxidation reaction (WOR). In previous studies, it has been shown that the presence of azole structures favors production of superoxide radical ($\cdot O_2^-$)[14], which is an important intermediate of ORR to produce $H_2O_2$. More significantly, the investigation reported by Wu *et al.* revealed that COF's benzoxazole moiety was reaction's active location for producing reactive oxygen species[15]. This offers encouraging evidence for investigating the logic and viability of construct-effect relationship's formation.

There are about thirty publications published in recent years on $H_2O_2$ production using COFs as photocatalyst, and their $H_2O_2$

10.1002/anie.202309480




production conditions and yields are summarized in the following table (Table S2). Single functional units such as pyrene, diarylamine, pyridine, diacetylene, and sulfone have been proven to be advantageous as active sites for photocatalytic $H_2O_2$ production[16]. Particularly, the presence of pyridine and diacetylene structures enables water oxidation to generate h $H_2O_2$. Introducing sulfone units achieves a transition from two-steps ORR to one step ORR for producing $H_2O_2$.

The incorporation of functional groups in ligands affects the yield, for instance, F-substitution alters crystallinity, mesoporous structure, and Lewis acid sites of COFs, thus affecting the ORR, optoelectronic properties and photocatalytic performance[17]. The hydroxyl group can efficiently traps holes ($h^+$), minimizes photo-generated carrier recombination, and enhances stability[18]. The existence of cyanide groups induces excitation of oxygen into a triple state $^1O_2$, rather than forming an intermediate $\cdot O_2^-$, accelerating the generation of $H_2O_2$[19].

Tetrathiafulvalene and benzothiazole formed a better synergistic effect and achieved a higher yield in the dual pathway $H_2O_2$ production conditions due to the rational design of ORR and WOR centers[20]. Using the *s*-heptazine and triazine moieties as the double oxygen reduction centers, and the benzene as WOR centers, the COF achieve a higher yield in the dual pathway $H_2O_2$ production conditions[21]. By using high-throughput sonication synthesis method, more than 60 kinds of COFs were prepared and tested for their ability to generate $H_2O_2$, among which sonoCOF-$F_2$ displayed excellent $H_2O_2$ generation performance. After prolonged photocatalytic testing, this COF underwent degradation. To improve its photo-stability, benzyl alcohol (BA) was introduced and modified, resulting in at least one week of stable $H_2O_2$ generation[22].

Previous reports shared our basic starting point of concentrating on the influence of micro-structural changes on photoelectrochemical properties and photocatalytic performance. The development of linkage chemistry in the research area of COFs is fundamentally important for creating robust structure with high crystallinity and diversified functionality in terms of photo-isomerization, narrow bandgap, Lewis base property, and redox activity. It remains a formidable challenge in developing linkages chemistry to uncover new rule in terms of connectivity and functionality. However, little known has been shown about the effect of linkage chemistry of COFs as functional basis to photoelectrochemical properties and photocatalysis. Filling the gap between linkage chemistry and photoelectrochemical application is extremely important and urgent for advancing the rational design and wide application of COFs.

Thus, a tunable COF platform with three structurally similar but linked by imidazole, oxazole and thiazole respectively (named as IZ-COF, OZ-COF, TZ-COF), are successfully constructed by linker substitution (Figure 1). For the first time, we successfully obtain highly crystalline imidazole-linked COFs via a linker exchange reaction involving the conversion of imine to oxazole and thiazole linkages. The results of photoelectrochemical analysis show that heteroatom differences affect visible light absorption, electron-hole separation complexes, carrier migration, and other properties. This information along with D-π-A structural analysis leads to the inference that photocatalytic properties are sorting by the sequence of TZ-COF > OZ-COF > IZ-COF. Subsequently, this inference was supported by the findings of a practical study of photocatalytic $H_2O_2$ production. In-depth mechanistic research revealed that three COFs produce $H_2O_2$ by reducing $O_2$ with a bonus that they both can generate $O_2$ on their own using $h^+$. Furthermore, the interfacial properties and active site of COFs are thoroughly investigated in order to conduct a thorough analysis of entire reaction process.

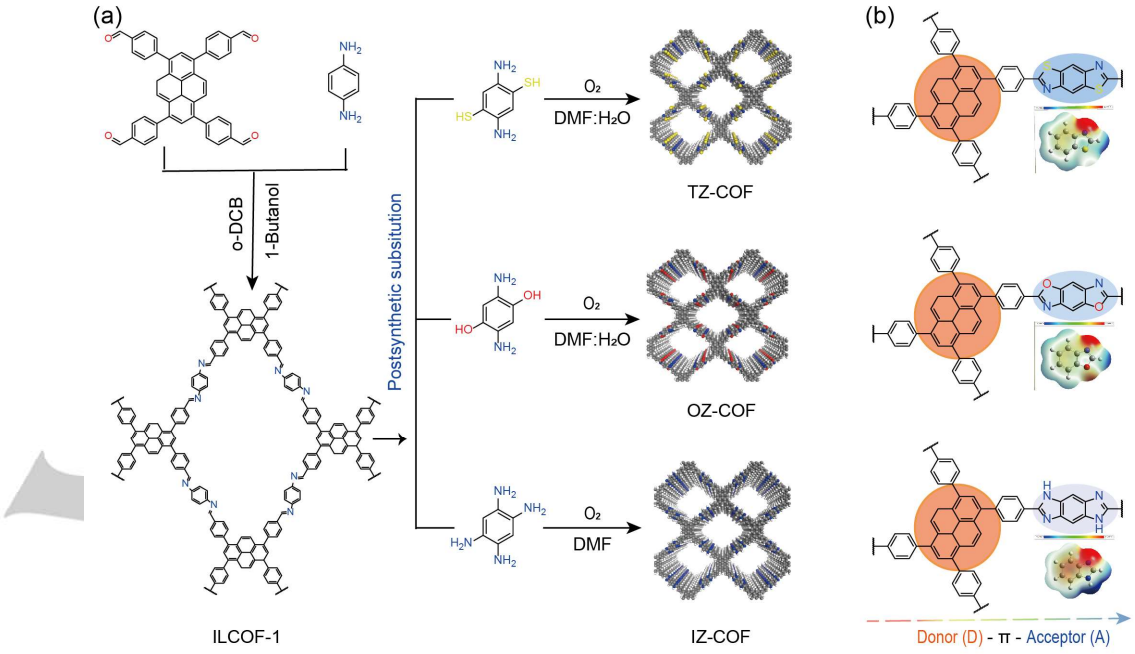


**Figure 1.** Synthetic routes (a), and (b) D-π-A model and differences of COFs with azoles linkages (the inset is the local charge distribution of azole fragments with the scale range from red to blue for 0.03 to -0.03).

## Results and Discussion

A quadrilateral topology was chosen for design of azoles-linked COFs as it permits π-conjugation along the x and y axes to communicate π-cloud overlap on a two-dimensional (2D) skeleton. The synthesis of imidazole-linked COFs was achieved by linker substitution, following a similar approach as that for synthesis of oxazole and thiazole linkages, as detailed in the Supplementary Information. The powder X-ray diffraction (PXRD) patterns

10.1002/anie.202309480




revealed that TZ-COF, OZ-COF, and IZ-COF were highly crystalline polymers (Figure 2a-2c). The IZ-COF exhibited diffraction peaks at 3.66°, 7.44°, 11.24° and 23.36° assigned to (110), (220), (330) and (001) plane. Similarly, TZ-COF and OZ-COF correspond to the peaks of these, were 3.72°,7.52°, 11.32°, 23.52° and 3.74°, 7.60°, 11.48°, 23.80°, respectively. The experimentally observed curves can be closely reproduced by Pawley refinement. And the results show that all COFs have A-A stacking mode. The grain sizes of TZ-COF, OZ-COF, IZ-COF calculated from half-peak width of (110) are 24.45 nm, 22.86 nm and 21.42 nm, respectively, as deduced from Scherrer formula[23], confirm more ordered and conjugated structure in TZ-COF (Figure S3a)[24]. Besides, the offset of position for (001) plane from 23.36, 23.52, to 23.80 for IZ-COF, TZ-COF to OZ-COF confirms that layer spacing follows the pattern IZ-COF>TZ-COF>OZ-COF, which is a direct response to degree of π-π stacking (Figure S3b).

The key structural character in valid linkage of COFs was verified by Fourier transform infrared (FT-IR), solid-state $^{13}C$ nuclear magnetic resonance (NMR) and X-ray photoelectron (XPS) spectra. The thiazole rings can be confirmed by observed peaks at 962 $cm^{-1}$ in TZ-COF, while the stretching vibration of oxazole ring is considered to be the consequence of peaks at 1590 and 1056 $cm^{-1}$ in OZ-COF (Figure 2d). From Figure S4, the detected peaks at 1622 $cm^{-1}$ (C=N), NH stretching ranging from 3412 $cm^{-1}$ (free NH) to 3200 $cm^{-1}$ (hydrogen bonded, NH) in IZ-COF serve as evidence of the presence of imidazole rings [25]. The TZ-COF showed signals in $^{13}C$ NMR spectra that come from the carbon atoms of thiazole rings at 167, 152, and 141 ppm (Figure 2e). The 163, 140, and 148 ppm signals for OZ-COF represent C atoms on oxazole ring. Similarly, the presence of 150 and 141 ppm signal from azole ring's C atom confirms the formation of imidazole ring in IZ-COF.

The C1s XPS spectra can be divided into three peaks, where except for the essential $sp^2$ aromatic (284.8 eV), C=N-C (285.8 eV), the unique peaks for TZ-COF are C-S-C (286.4 eV), C-O-C (286.9 eV) for OZ-COF, and C-N-C (290.6 eV) for IZ-COF (Figure S5). Particularly, the presence of a double peak in N1s curve of IZ-COF confirms the presence of two distinct bonding states N, C-N-C (400.4 eV) and C=N-C (398.7 eV) while OZ-COF and TZ-COF contain only C=N-C. The presence of S signal in full spectrum comparison, as well as the delineation of 165.2 (2p1/2) and 163.9 eV (2p3/2) spin-orbital peaks in S 2p spectrum, point to the formation of TZ-COF. All of these findings provided strong support for the formation of imidazole-, oxazole-, and thiazole-linked COFs.

Porosity was investigated using $N_2$ adsorption-desorption isotherm measurements. Three COFs appear as type I sorption curves (Figure 2f). The Brunauer–Emmett–Teller surface areas of TZ-COF, OZ-COF and IZ-COF were measured as 451, 690, and 740 $m^2\ g^{-1}$. And pore size distributions calculated by using non-linear density functional theory (DFT) show that they are all mesoporous polymers with sizes of 2.21, 2.24, and 2.14 nm, respectively (Figure S6). Those results give solid evidences that three kinds of COFs with favorable crystalline and porosity had been successfully prepared.

Employing a combination of scanning electron microscopy and transmission electron microscopy (TEM) reveals the unique morphological characteristics (Figure S7), which are granular, sheet and rod-like, for TZ-COF, OZ-COF and IZ-COF respectively. The clear dark and light stripes produced by high-resolution TEM corresponding to the interlayer space with the distances of 0.365, 0.362 and 0.377 nm for TZ-COF, OZ-COF and IZ-COF, respectively. It also ascribes to the (001) plane, which reinforced the degree of longitudinal π-π interaction follows the order of IZ-COF < TZ-COF < OZ-COF. Besides, the hydrophobicity is significantly impacted by heteroatomic alterations [26]. The contact angles of COFs are in the following order of OZ-COF (50°) < IZ-COF (65°) < TZ-COF (125°) (Figure S8). These data highlight the effect of different linkages on the microstructure and surface/interface of COFs.

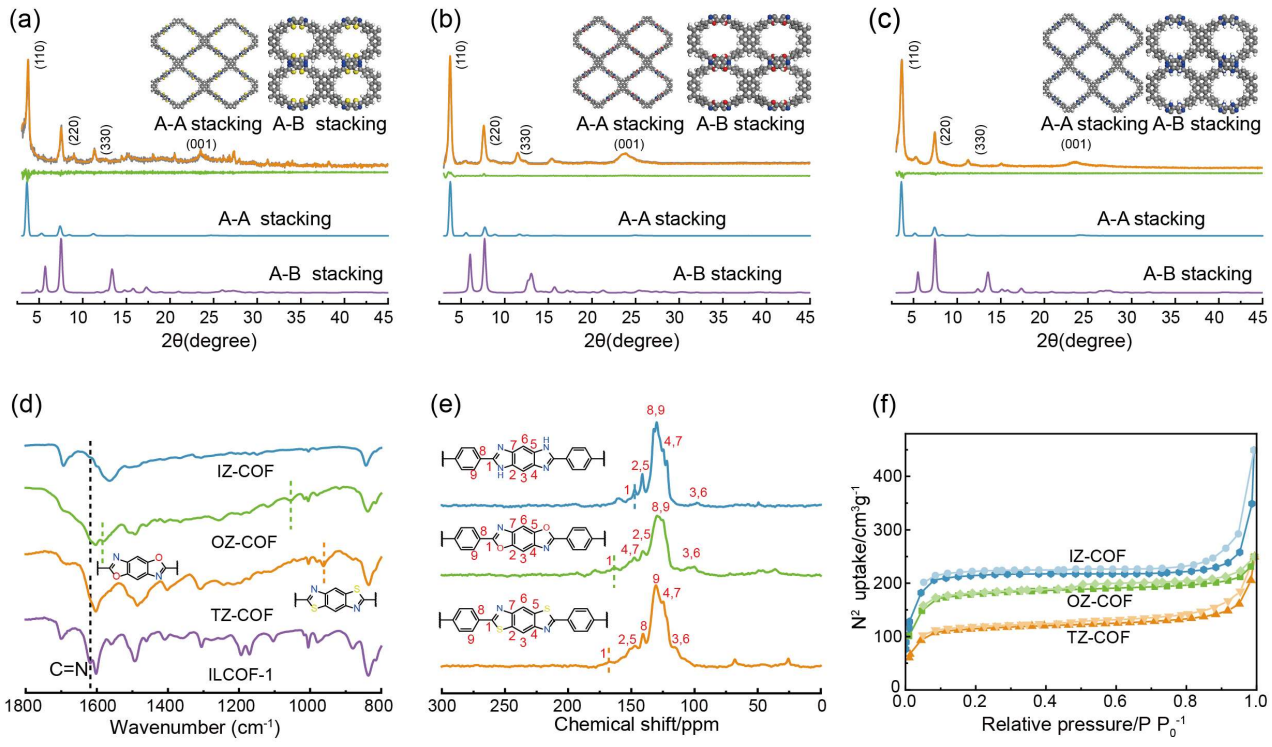


**Figure 2.** Experimental and simulated PXRD patterns (a-c), FTIR (d), solid-state $^{13}C$ NMR spectra (e) and $N_2$ sorption isotherms (f) for TZ-COF, OZ-COF, IZ-COF.

10.1002/anie.202309480


RESEARCH ARTICLE

The ultraviolet–visible diffuse reflectance spectra were used to examine the photophysical characteristics of COFs first. As seen in Figure S9, the yellow-brown IZ-COF, dark-brown OZ-COF, and dark-green TZ-COF established similar wide visible light absorption but notable variations in maximum absorption band, causing the band gaps offsets of 2.12, 2.04, and 1.98 eV, respectively (Figure S10). The increase in along and across the plane conjugation is the primary cause of visible light absorption capacity[17]. The electron density in thiazole ring of TZ-COF is more evenly distributed between S and C atoms due to differences in electronegativity and the presence of an empty d orbital in S. Consequently, the electrons in TZ-COF are more readily delocalized in π orbitals along the plane of conjugation, compared to those of IZ-COF and OZ-COF[27]. For across the plane conjugation, the order of conjugated strength in extend framework is OZ-COF>TZ-COF>IZ-COF which can be proven by layer spacing from PXRD and TEM. Combined, TZ-COF has the strongest degree of conjugation, thus establishing the widest absorbance range. VB-XPS was used to determine the positions of valence bands for COFs with 1.67, 1.68, and 1.35 eV for IZ-COF, OZ-COF, and TZ-COF, respectively (Figure S11-12). Thus, azole linkages in the extended framework change both visible-light absorption capacity and redox potentials, offering a special point of view for improving the photocatalytic performance of COFs.

The self-contained planar benzene ring unit in 1,3,6,8-Tetrakis(4-formylphenyl)pyrene (TFPPy) acts as a π crosslinker, while the donor unit of pyrene and the azole linkage build the acceptor unit effectively facilitating charge transport and separation of $h^+$ from charriers[28]. The photoelectrochemical properties enhanced by overall D-π-A structure were confirmed by electrochemical tests and photoluminescence (PL) spectra (Figure S9). Smaller semicircle of electrochemical impedance spectroscopy (EIS) substantially further demonstrated TZ-COF reduced internal charge transfer resistance compared with the OZ-COF and IZ-COF. TZ-COF demonstrated a quicker photoresponse with a photocurrent density of 3.82 μA $cm^{-2}$ compare to OZ-COF and IZ-COF (1.26 and 0.63 μA $cm^{-2}$). This finding suggests that the photoinduced charges transfer in TZ-COF is more effective. The emission peaks of both OZ-COF and TZ-COF showed red-shift and substantially quenched intensities in comparison to the PL spectra of IZ-COF, indicating greatly suppressed recombination of photogenerated electron-hole pairs.

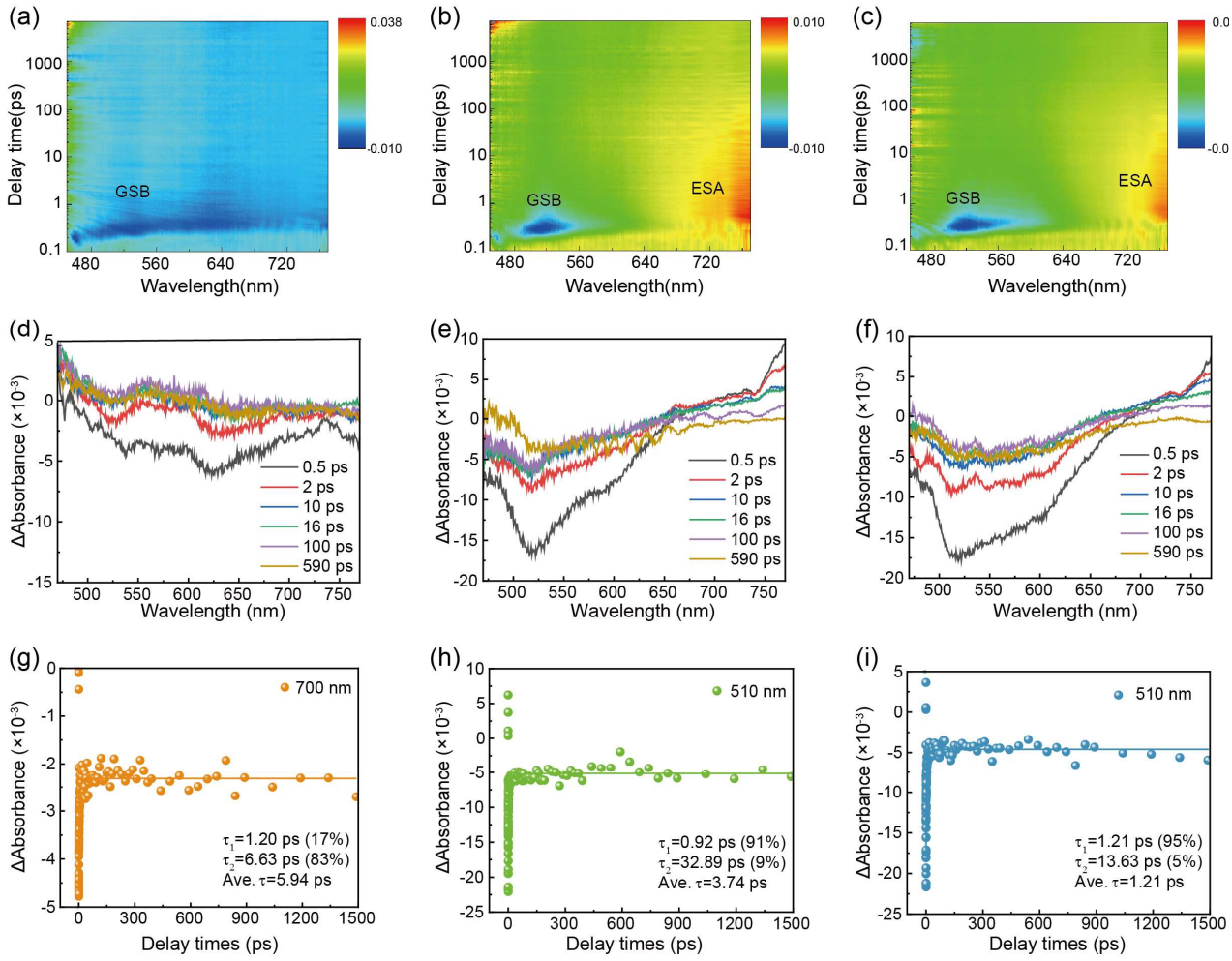


**Figure 3.** 2D mapping TA spectra of (a-c), TA spectra signals on the fs-ns timescales (d-f) and decay kinetic curves (g-i) of TZ-COF, OZ-COF and IZ-COF.

Femtosecond time-resolved transient absorption (fs-TA) spectroscopy was used to investigate photoexcited carrier dynamics. As shown in Figure 3, TZ-COF showed obvious ground state bleach (GSB) signals at 540nm and stimulated emission around 625 nm, basically recovered within 10 ps. The GSB signal was caused by neutral singlet excitation, associated with characteristic simulated emission. OZ-COF and IZ-COF exhibited extensive excited state absorption (ESA) feature that developed on ultrafast time scales. The ESA with center of 760 nm appeared immediately after the photoexcitation of OZ-COF, attributing to electron excitation formation. A negative peak can be observed at 740 nm for OZ-COF and IZ-COF, which are reasonably interpreted as a photoinduced emission process originating from the interfacial charge transfer from TFPPy to oxazole/imidazole linkage According to the kinetics of COFs, TZ-COF has a much longer-lived excited state absorption decay of 5.94 ps than OZ-COF(3.74 ps) and IZ-COF(1.86 ps), which is consistent with the high efficiency of charge separation and transfer [29]. It is also strongly correlated with the D-π-A effects of azoles-related linkages in COFs.

Substitution of electron acceptors has been proven to effectively regulate electron-hole separation due to electronegativity differences[30]. But, the electronegativity order of N>S>O cannot explain the photoelectricity. The structural differences lie mainly in the pyrrole-like heteroatom on five-membered ring, which exhibit electron-absorbing inductive effects and electron-donating effects, and the conjugated effect was stronger than inductive effect[31]. Less cross-cap is visible between the 2p orbital of C atom and 3p orbital of S atom, implying lessen contribution of electrons in azole ring, disrupting the order of electron-donating effect[32]. Thus, the photoelectric performance follows the order of TZ-COF > OZ-COF > IZ-COF. Besides, an increase in the domain of π-electron delocalization boost carrier migration and thus the conductivity of COFs, resulting in a decrease in EIS semicircle diameter[33]. The combination of broadening light absorption and enhanced electrical conductivity excites strong photocurrents. These indicate that the more accessible channels of charge transfer were constructed in TZ-COF via D-π-A structure between thiazole linkage and pyrene linker, leading to efficient suppression of photoexcited charge recombination.

All COFs were tested for photocatalytic $H_2O_2$ generation performance under λ > 420 nm illumination in pure $H_2O$ without any sacrificial agents. As shown in Figure 4a, with the increase of catalyst concentration from 0.5 to 1.5 g $L^{-1}$, the yield of $H_2O_2$ enhances. Upon the catalyst concentration exceeds to 1.5 g $L^{-1}$, it appear a downward trend, which was ascribed the shield effect of high-concentration catalyst for visible light absorption (Figure S13)[34]. Based on the optimum concentration, IZ-COF displayed an $H_2O_2$ production rate of 102 μmol $h^{-1}g^{-1}$, which was increased to 220 μmol $h^{-1}$ $g^{-1}$ for OZ-COF and 268 μmol $h^{-1}$ $g^{-1}$ for TZ-COF (Figure 4b). Similar trends were also seen in comparison of solar-to-chemical conversion (SCC) efficiency, where TZ-COF having the highest value of 0.036%. TZ-COF displayed an apparent quantum (AQY) of 0.6% at 475 nm (Figure S14). In a 1:1 ratio of water and $CH_3OH$ system, TZ-COF exhibits a 1.44-fold rate increase (from 268 to 386 μmol $g^{-1}$ $h^{-1}$), and an 18.48-fold rate increase (to 4951 μmol $g^{-1}$ $h^{-1}$) in a 1:1 ratio of water and BA system compared with the water system. The enhancement may be that in a two-phase system, the $H_2O_2$ decomposition is severely inhibited as the active COFs sites remain in BA phase while the newly generated $H_2O_2$ diffuses into the water phase more quickly, allowing for a rise in concentration of $H_2O_2$ in water phase (Figure S15) [16a].

Subsequently, the $H_2O_2$ produced by TZ-COF was used in microbial sterilization experiments, and it was clearly observed that the growth of *Escherichia coli* was efficiently inhibited (Figure S16). After three cycles, the $H_2O_2$ generation rate of TZ-COF reduced. The XRD and FT-IR of COFs after cycling revealed no major changes in chemical components but a reduction in crystallinity. (Figure S17-19). A follow-up study on the effect of crystallinity on photocatalytic performance (Figure S19-20) suggests that crystallinity is a contributing factor, but overall photocatalytic performance was influenced by multiple factors such as wettability, surface charge and so on.

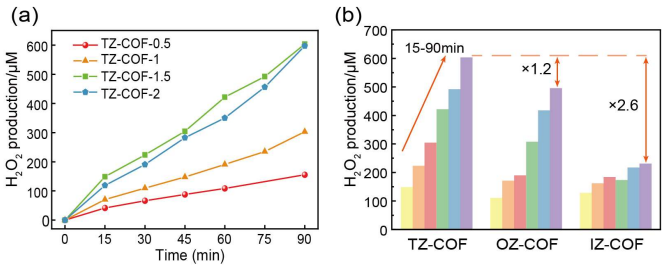


**Figure 4.** (a) $H_2O_2$ yield rates of TZ-COF with different concentrations (TZ-COF-0.5 represents a catalyst concentration of 0.5 g $L^{-1}$). (b) $H_2O_2$ yields of COFs dispersed in $H_2O$ at a concentration of 1.5 g $L^{-1}$.

The reaction pathways over COFs are examined to shed light on the mechanism underlying increased photocatalytic $H_2O_2$ production. As seen in Figure 5a, and S21, the significant decrease in yield observed upon removing $O_2$ by blowing Ar, coupled with the low $H_2O_2$ yields obtained using $KBrO_3$ as an electron trapping agent, confirms the involvement of $O_2$ as a reactant in production of $H_2O_2$. Furthermore, in the presence of p-benzoquinone (BQ) as quenching of $\cdot O_2^-$, virtually little $H_2O_2$ created and a distinctive DMPO-$\cdot O_2^-$ signature appeared in electron paramagnetic resonance spectroscopy experiments using 5,5-dimethyl-1-pyrrole n-oxide (DMPO) as a spin trap agent to capture $\cdot O_2^-$(Figure S22a). The yield of $\cdot O_2^-$, quantified by characteristic reaction with Cytochrome C[35], for TZ-COF was $0.76\times10^{-5}$ M, significantly higher than that of OZ-COF ($0.64\times10^{-5}$ M) and IZ-COF($0.55\times10^{-5}$ M) (Figure S22b), indicating thiazole linkage facilitated the formation of $\cdot O_2^-$ intermediates. The rotating disk electrode (RDE) experiment results showed that average electron transfer number of ORR was 2.03, 1.67, and 1.11 on IZ-COF, TZ-COF and OZ-COF, respectively, which confirmed 2e- reaction process (Figure 5b and S23). And the transfer electron number approaching 1 is more inclined to single electron reduction pathway, affecting the conversion of $\cdot O_2^-$ to $H_2O_2$ [36].

10.1002/anie.202309480




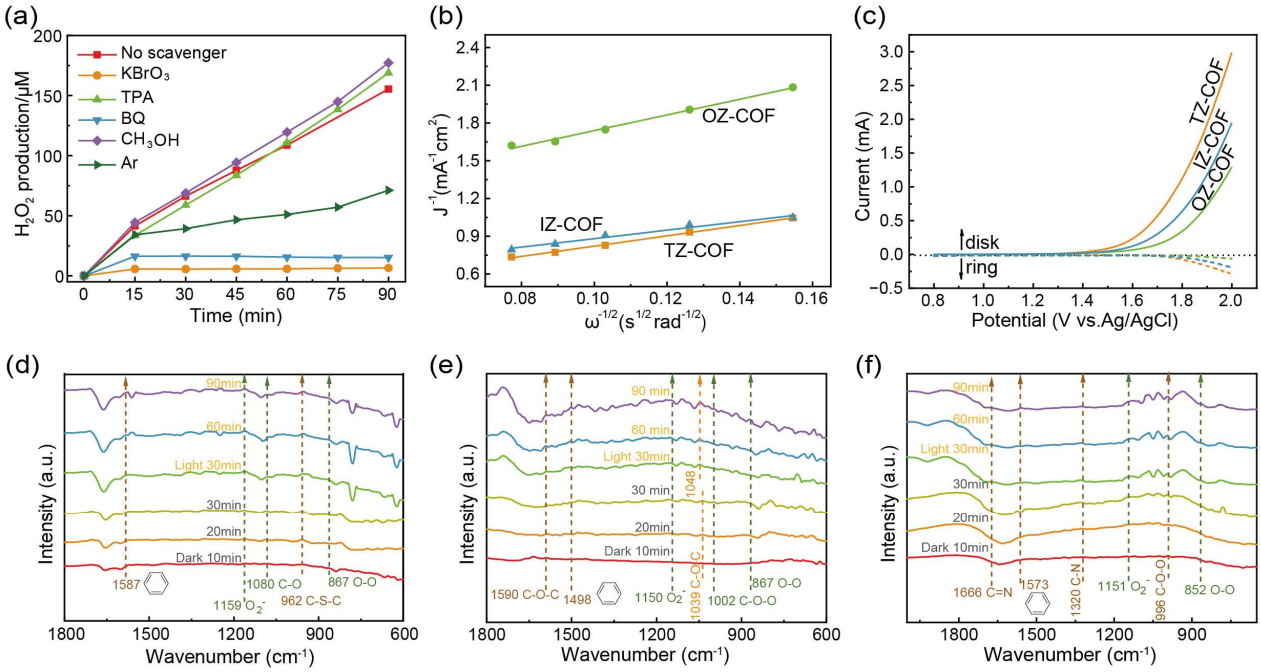


**Figure 5**. (a) Comparison of $H_2O_2$ evolution catalyzed by TZ-COF in the presence and absence of scavengers. (b) The Koutecky–Levich plots obtained by RDE measurements *Vs.* Ag/AgCl. (c) RRDE voltammograms obtained in 0.1 M phosphate buffer solution with a scan rate of 10 mV $s^{-1}$ and a rotation rate of 1000 rpm. The potential of the Pt ring electrode is set at -0.23 V versus Ag/AgCl to detect $O_2$. Photocatalytic mechanism of $H_2O_2$ synthesis in TZ-COF (d), OZ-COF (e) and IZ-COF (f) based on in situ FT-IR.

After $O_2$ was removed, the yield was not completely suppressed, prompting the exploration of WOR pathway. When $CH_3OH$ and tert-butanol (TPA) were respectively added as $h^+$ and hydroxyl radical trapping agent, the rate of $H_2O_2$ production increased. This may be because either the capture of $h^+$ provides more photogenerated electrons to participate in ORR or the presence of alcohols provides an alternative pathway for $\cdot O_2^-$ to obtain *H, thus facilitating the production of $H_2O_2$[37]. This phenomenon denies the conjecture that $H_2O_2$ production from WOR and enhances the possibility of $O_2$ production. Subsequently, the production of $O_2$ was measured by rotating ring-disk electrode (RRDE) under Ar, and the experimental results verified that these COFs were able to produce $O_2$ (Figure 5c). Similar phenomenon has been reported by Xu et al.[9]

The nature of surface/interface should be studied because it has a significant impact on the interfacial catalytic kinetics, which directly affects the effectiveness of photocatalysts. Firstly, the strong hydrophobicity in TZ-COF may lead to obtain $O_2$ from air, where the $O_2$ concentration of approximately much higher than that of $H_2O$, and an enhanced diffusion rate of $O_2$ can be achieved on the catalyst surface[38]. In addition, hydrophobicity facilitates the separation of $H_2O_2$ from surface of COFs , in turn availing the reaction toward positive direction[39]. Second, the reduction current of RRDE is most pronounced on TZ-COF, indicating more $O_2$ generation and creating a better $O_2$-rich atmosphere for $2e^-$ ORR. Moreover, more photoinduced $h^+$ are utilized on TZ-COF, facilitating the extraction of electron-hole equilibrium and suppressing partial electron-hole complexation, resulting in better photocatalytic performance[40]. Finally, Zeta potential was used to characterize the surface affinity of COFs for $H^+$. Figure S24 shows that TZ-COF (-17.0 mV) and OZ-COF (-21.8 mV) have a more negative Zeta potential than IZ-COF (27.6 mV), indicating that they have a stronger electrostatic attraction toward $H^+$.

*In situ* diffuse reflectance infrared fourier transform spectroscopy was additionally used to confirm functional group changes that occurred during reactions. In dark, mild infrared vibrations appear at around 867 and 1080 $cm^{-1}$ for all COFs, this gives a credit for $O_2$ adsorption. Under illumination, as shown in Figure 5d, for TZ-COF, the intensity of peaks at 1587 $cm^{-1}$ and 962 $cm^{-1}$ were gradually increasing along with new peaks at 1159 $cm^{-1}$ appeared. Figure 5e for OZ-COF illustrates the increased peak intensity at 1498 $cm^{-1}$, the blueshift from 1039 to 1048 $cm^{-1}$, and the emerging peak at 1150 $cm^{-1}$. In Figure 5f, for IZ-COF, the intensity of peaks at 1573, 1320 and 1666 $cm^{-1}$ enhanced, while new peaks at 1151 $cm^{-1}$ appeared in photocatalytic phase. The reactive benzene rings and linkage bonds are responsible for the raised peaks and the formation of $\cdot O_2^-$ results in the appearance of new peaks. Based on above analysis, we infer that the possible $O_2$ adsorption sites of COF's (Figure S25) including benzene ring fragment between pyrene unit and azole linkages (site 1), azole linkage (site 2), benzene between azole linkages (site 3) and pyrene (site 4).

10.1002/anie.202309480

WILEY-VCH

RESEARCH ARTICLE

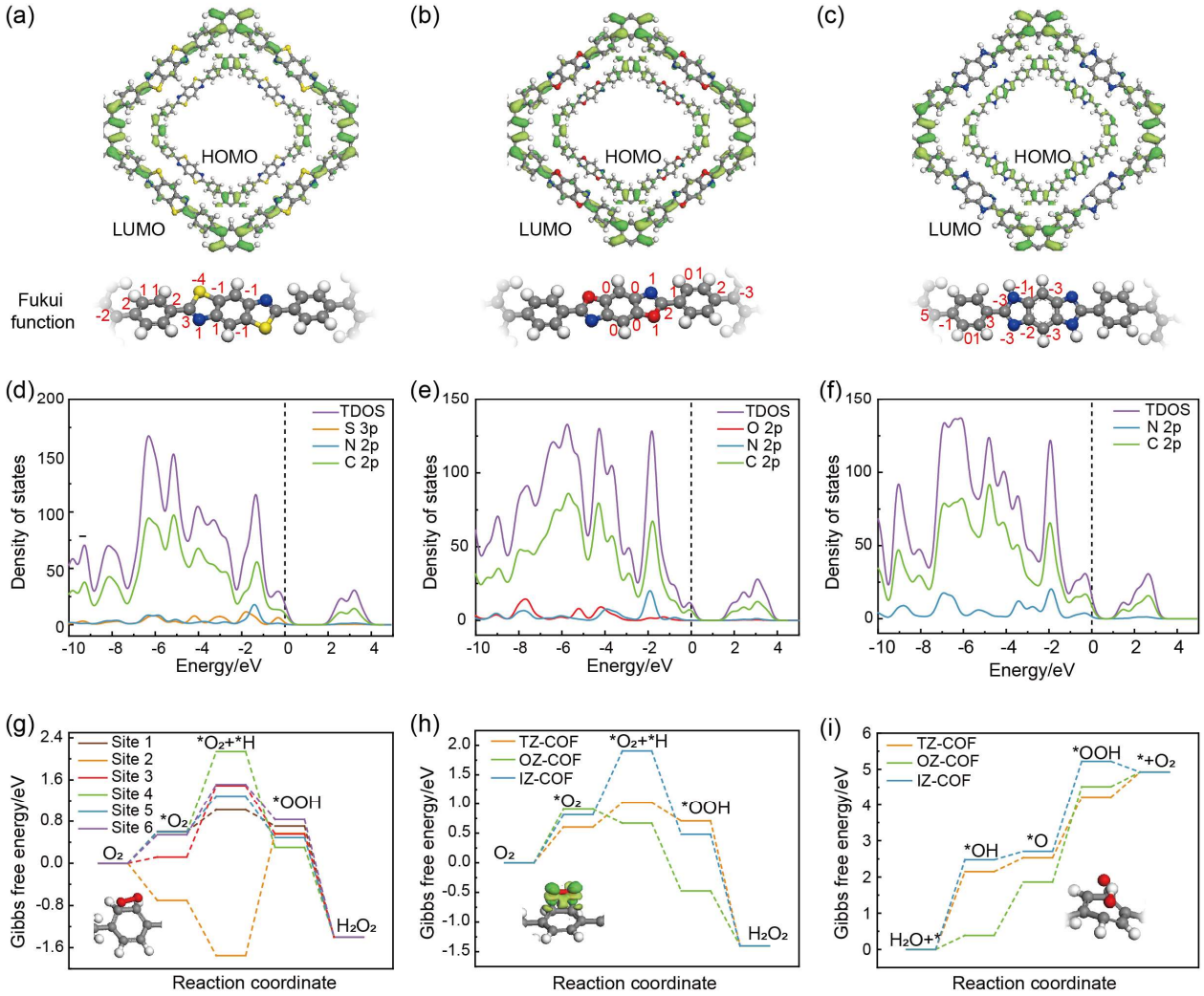


**Figure 6.** Calculated HOMO and LUMO distribution and the $fi^{(2)}$ obtained using the Fukui function of TZ-COF, OZ-COF, IZ-COF(a-c) (the specific value of $fi^{(2)}$ is the value in the graph multiplied by $10^{-3}$). Total (TDOS) and partial density of states (PDOS) for TZ-COF (d), OZ-COF (e) and IZ-COF (f). (g) ΔG at different $O_2$ adsorption sites of TZ-COF, (h) ΔG for ORR and (i) WOR of three COFs (small diagrams are structure diagrams or differential charge distribution diagrams).

To further refine the analysis, we calculated the highest occupied molecular orbital (HOMO) and the lowest unoccupied molecular orbital (LUMO) with the help of Dmol3. The HOMO of both TZ-COF and OZ-COF were distributed on pyrene unit, while IZ-COF differed in that its HOMO orbital was also distributed on imidazole ring (Figure 6a-c). The LUMO of three COFs are dispersed where the pyrene is attached to azole unit, confirming the previous design of electron-donator for pyrene and electron-acceptor for azole linkage. And the density of states calculations show that heteroatoms (S, O and N) are involved in the construction of HOMO in azole-linkage, confirming the rationality of the analysis from electron-donating effect[41] (Figure 6d-f). The electron-definition function further confirms that azole linkage confers a large degree of conjugation to the structure (Figure S26). The dual descriptor ($fi^{(2)}=fi^{(+)}-fi^{(-)}$) of Fukui function combines the electrophilic ($fi^{(-)}$) and nucleophilic ($fi^{(+)}$) parameters, with its >0 indicating susceptibility to nucleophilic attack[42]. Oxygen intermediates tend to bind to nucleophilic sites, which are mostly attributed to Site 1, thus confirming from the side that the reaction site may prefer to be present here.

DFT calculations were performed to investigate the formation pathway of $H_2O_2$ on TZ-COF. The $2e^-$ ORR pathway on TZ-COF is associated with the protonation of possible intermediates of oxygen molecules such as $*O_2$, $*O_2$+*H, and *OOH. As shown in Figure 6g, the corresponding adsorption energy for sites 1-4 and additional marginal sites 5,6 was calculated (Figure S25). And the results indicated that only site 1 had a favorable adsorption energy with the value of -2.43 eV, indicating that this part was presented as a favorable site for the adsorption and conversion of $O_2$. And the sites 5,6 used as a comparison did not show lower adsorption energy, indicating that the reaction takes place at the periodic COF structure. According to the differential charge density diagram, it is known that $O_2$ acquires electrons from the benzene sites in a state parallel to benzene ring (Figure S27).

Correspondingly, Gibbs free energy change (ΔG) for each step involved in $2e^-$ ORR was calculated according to the optimized structure, as depicted in Figure 6h and S28. The rate-limiting step for OZ-COF is the conversion of $O_2$ to $*O_2$, which exhibits an extremely high energy barrier of 0.91 eV. Consequently, the timely conversion of adsorbed $O_2$ onto active sites to $*O_2$ is impeded, thus adversely affecting the subsequent site response. IZ-COF, besides, weakened the adsorption of $*O_2$ intermediate with a ΔG value of 0.82 eV. However, it exhibits a relatively high free energy (1.09 eV) during the protonation to form $*O_2$/*H intermediate. Optimally, TZ-COF simultaneously modulates the binding strength of $*O_2$ and $*O_2$/*H intermediate,

thereby promoting 2e⁻ ORR with a lower energy barrier of 0.61 eV. This outcome confirmed that the order of $H_2O_2$ production by ORR follows the rule of TZ-COF > OZ-COF > IZ-COF. With regard to 4e⁻ WOR pathway occurring on OZ-COF and IZ-COF, the *OOH generation from *O is the most vital step, with a value of 2.65 and 2.51 eV (Figure 6i), respectively. The thiazole linkage affects the molecular orbitals of TZ-COF, giving it a lower energy barrier to form *O and maintaining a minimum ΔG (2.15 eV) in rate-limiting step ($H_2O$+* → *OH). The ΔG of WOR was also considered, effectively supporting the law obtained RRDE results.

In summary, $H_2O_2$ photosynthesis in this system is as follows. Under visible light conditions, COFs were excited to produce photogenerated electrons and $h^+$. The electron-rich pyrene region server as light-absorber and donor unit and the azole linkage acts as an acceptor. This induces the electron directional transfers frompyrene region to azole fragments. Different electron-donating conjugated effects of azoles linkage via constructed D-π-A structure vary the visible light absorption, energy band tuning, photogenerated carrier migration. In the presence of $O_2$, the benzene ring fragment between pyrene unit and azole linkage are anchoring $O_2$ via electron donor-acceptor complex reaction, which combinate the excited photoelectrons to generate $\cdot O_2^-$. It further combines with the proton from $H_2O$ to selectively produce *OOH intermediate for the formation of $H_2O_2$. Moreover, the photoinduced $h^+$ over oxidize $H_2O$ to generate $O_2$, which is benefit to replenish $O_2$ for $H_2O_2$ production under the condition of low or no $O_2$ concentration, showing that the photocatalysts are highly stable and recyclable.

## Conclusion

In conclusion, for the effective production of $H_2O_2$, we conducted a systematic study on the azole-linked COFs. Our findings demonstrated that thiazole is the most effective linkage among all of them. The linkage microenvironment of azole-linked COFs, which vary the crystal structure, electronic effects, surface interface properties, etc., also plays a significant role in improving the photocatalytic performance. The findings demonstrate that thiazole linkage results in a wider visible light absorption, a narrower band gap, and more effective electron-hole separation. Thus, the $H_2O_2$ production rate goes in the following order: TZ-COF>OZ-COF>IZ-COF. According to DFT calculations, linkage chemistry, which increases the activities of nearby benzene rings, made it easier to form the appropriate intermediates for the 2e⁻ ORR, which produces $H_2O_2$. In addition, as a recharge for ongoing $H_2O_2$ production, the accumulated $h^+$ quicken the oxidation of $H_2O$ to form $O_2$. Developing highly effective photocatalytic systems can be accomplished through the precise regulation of linkage microenvironment in porous periodically organic network.

## Acknowledgements

The authors gratefully acknowledge the financial support provided by the National Natural Science Foundation of China (No. 22178091, 72088101 and 52202367), Provincial Natural Science Foundation of Hunan (No. 2023JJ10012), the Science and Technology Innovation Program of Hunan Province (No. 2022RC1120), the Natural Science Foundation of Jiangsu Province (BK20200711), and the Fundamental Research Funds for the Central Universities (No. 531118010675).

**Keywords:** Azoles linkage • COFs • $H_2O_2$ • Photocatalysis.

[1] a) H. Wang, C. Qian, J. Liu, Y. Zeng, D. Wang, W. Zhou, L. Gu, H. Wu, G. Liu, Y. Zhao, *J. Am. Chem. Soc.* **2020**, *142*, 4862–4871; b) J. Niu, L. Li, Y. Wang, J. Su, J. Li, X. Wang, *Science.* **2018**, *52*, 48–52; c) C. Gropp, T. Ma, N. Hanikel, O. M. Yaghi, *Science.* **2020**, *370*, eabd6406.

[2] a) H. Wang, Y. Yang, X. Yuan, W. Liang Teo, Y. Wu, L. Tang, Y. Zhao, *Mater. Today* **2022**, *53*, 106–133; b) Q. Zhang, S. Dong, P. Shao, Y. Zhu, Z. Mu, D. Sheng, T. Zhang, X. Jiang, R. Shao, Z. Ren, J. Xie, X. Feng, B. Wang, *Science*. **2022**, *378*, 181–186.

[3] M. R. Rao, Y. Fang, S. De Feyter, D. F. Perepichka, *J. Am. Chem. Soc.* **2017**, *139*, 2421–2427.

[4] L. Cusin, H. Peng, A. Ciesielski, P. Samorì, *Angew. Chem. Int. Ed.* **2021**, *60*, 14236–14250.

[5] P. F. Wei, M. Z. Qi, Z. P. Wang, S. Y. Ding, W. Yu, Q. Liu, L. K. Wang, H. Z. Wang, W. K. An, W. Wang, *J. Am. Chem. Soc.* **2018**, *140*, 4623–4631.

[6] R. Paul, S. Chandra Shit, H. Mandal, J. Rabeah, S. S. Kashyap, Y. Nailwal, D. B. Shinde, Z. Lai, J. Mondal, *ACS Appl. Nano Mater.* **2021**, *4*, 11732–11742.

[7] S. Nandi, S. K. Singh, D. Mullangi, R. Illathvalappil, L. George, C. P. Vinod, S. Kurungot, R. Vaidhyanathan, *Adv. Energy Mater.* **2016**, *6*, 1601189.

[8] M. Deng, J. Sun, A. Laemont, C. Liu, L. Wang, L. Bourda, C. Jeet, K. Van Hecke, R. Morent, N. De Geyter, K. Leus, H. Chen, P. Van Der Voort, *Green Chem.* **2023**, *25*, 3069–3076.

[9] H. Cheng, H. Lv, J. Cheng, L. Wang, X. Wu, H. Xu, *Adv. Mater.* **2022**, *34*, 2107480.

[10] F. Yu, Z. Zhu, S. Wang, Y. Peng, Z. Xu, Y. Tao, J. Xiong, Q. Fan, F. Luo, *Chem. Eng. J.* **2021**, *412*, 127558.

[11] F. P. Kinik, A. Ortega-Guerrero, D. Ongari, C. P. Ireland, B. Smit, *Chem. Soc. Rev.* **2021**, *50*, 3143–3177.

[12] C. Tantardini, A. R. Oganov, *Nat. Commun.* **2021**, *12*, 2087.

[13] Y. Kofuji, Y. Isobe, Y. Shiraishi, H. Sakamoto, S. Tanaka, S. Ichikawa, T. Hirai, *J. Am. Chem. Soc.* **2016**, *138*, 10019–10025.

[14] Y. H. So, J. M. Zaleski, C. Murlick, A. Ellaboudy, *Macromolecules* **1996**, *29*, 2783–2795.

[15] C. J. Wu, X. Y. Li, T. R. Li, M. Z. Shao, L. J. Niu, X. F. Lu, J. L. Kan, Y. Geng, Y. Bin Dong, *J. Am. Chem. Soc.* **2022**, *144*, 18750–18755.

[16] a) J. Sun, H. Sekhar Jena, C. Krishnaraj, K. Singh Rawat, S. Abednatanzi, J. Chakraborty, A. Laemont, W. Liu, H. Chen, Y. Y. Liu, K. Leus, H. Vrielinck, V. Van Speybroeck, P. Van Der Voort, *Angew. Chem. Int. Ed.* **2023**, *62*, e202216719; b) C. Krishnaraj, H. Sekhar Jena, L. Bourda, A. Laemont, P. Pachfule, J. Roeser, C. V. Chandran, S. Borgmans, S. M. J. Rogge, K. Leus, C. V Stevens, J. A. Martens, V. Van Speybroeck, E. Breynaert, A. Thomas, P. Van Der Voort, *J. Am. Chem. Soc.* **2020**, *142*, 20107–20116; c) M. Kou, Y. Wang, Y. Xu, L. Ye, Y. Huang, B. Jia, H. Li, J. Ren, Y. Deng, J. Chen, Y. Zhou, K. Lei, L. Wang, W. Liu, H. Huang, T. Ma, *Angew. Chem. Int. Ed.* **2022**, *61*, e20220413; d) L. Chen, L. Wang, Y. Wan, Y. Zhang, Z. Qi, X. Wu, H. Xu, *Adv. Mater.* **2020**, *32*, 1904433; e) Y. Luo, B. Zhang, C. Liu, D. Xia, X. Ou, Y. Cai, Y. Zhou, J. Jiang, B. Han, *Angew. Chem. Int. Ed.* **2023**, *62*, e202305355.

[17] H. Wang, C. Yang, F. Chen, G. Zheng, Q. Han, *Angew. Chem. Int. Ed.* **2022**, *61*, e202202328.

[18] Y. Yang, J. Kang, Y. Li, J. Liang, J. Liang, L. Jiang, D. Chen, J. He, Y. Chen, J. Wang, *New J. Chem.* **2022**, *46*, 21605–21614.

[19] X. Di, X. Lv, H. Wang, F. Chen, S. Wang, G. Zheng, B. Wang, Q. Han, *Chem. Eng. J.* **2023**, *455*, 140124.

[20] J. N. Chang, Q. Li, J. W. Shi, M. Zhang, L. Zhang, S. Li, Y. Chen, S. L. Li, Y. Q. Lan, *Angew. Chem. Int. Ed.*. **2023**, *62*, e202218868.

[21] D. Chen, W. Chen, Y. Wu, L. Wang, X. Wu, H. Xu, L. Chen, *Angew. Chem. Int. Ed.* **2023**, *62*, e202217479.

[22] W. Zhao, P. Yan, B. Li, M. Bahri, L. Liu, X. Zhou, R. Clowes, N. D. Browning, Y. Wu, J. W. Ward, A. I. Cooper, *J. Am. Chem. Soc.* **2022**, *144*, 9902–9909.

[23] J. Biscoe, B. E. Warren, *J. Appl. Phys.* **1942**, *13*, 364–371.

[24] W. Xu, Y. Gao, W. Ming, F. He, J. Li, X. H. Zhu, F. Kang, J. Li, G. Wei, *Adv. Mater.* **2020**, *32*, 2003965.

[25] K. C. Ranjeesh, R. Illathvalappil, S. D. Veer, S. Kurungot, S. S. Babu, *J. Am. Chem. Soc.* **2019**, 141, 14950–14954.

[26] V. Singh, J. Kim, B. Kang, J. Moon, S. Kim, W. Y. Kim, H. R. Byon, *Adv. Energy Mater.* **2021**, *11*, 2003735.

[27] M. Zhao, M. Samoc, P. N. Prasad, B. A. Reinhardt, M. R. Unroe, M. Prazak, R. C. Evers, J. J. Kane, C. Jariwala, M. Sinsky, *Chem. Mater.* **1990**, *2*, 670–678.

[28] Y. Xu, N. Mao, C. Zhang, X. Wang, J. Zeng, Y. Chen, F. Wang, J. X. Jiang, *Appl. Catal. B Environ.* **2018**, *228*, 1–9.

[29] C. Mo, M. Yang, F. Sun, J. Jian, L. Zhong, Z. Fang, J. Feng, D. Yu, *Adv. Sci.* **2020**, *7*, 1902988.

[30] Z. Zhao, Y. Zheng, C. Wang, S. Zhang, J. Song, Y. Li, S. Ma, P. Cheng, Z. Zhang, Y. Chen, *ACS Catal.* **2021**, *11*, 2098–2107.

[31] C. G. Zhan, D. A. Dixon, M. I. Sabri, M. S. Kim, P. S. Spencer, *J. Am. Chem. Soc.* **2002**, *124*, 2744–2752.

[32] K. E. Horner, P. B. Karadakov, *J. Org. Chem.* **2015**, *80*, 7150–7157.

[33] C. Lin, X. Liu, B. Yu, C. Han, L. Gong, C. Wang, Y. Gao, Y. Bian, J. Jiang, *ACS Appl. Mater. Interfaces* **2021**, *13*, 27041–27048.

[34] A. Torres-Pinto, M. J. Sampaio, C. G. Silva, J. L. Faria, A. M. T. Silva, *Appl. Catal. B Environ.* **2019**, *252*, 128–137.

[35] J. Butler, G. G. Jayson, A. J. Swallow, *Biochim. Biophys. Acta - Bioenerg.* **1975**, *408*, 215–222.

[36] S. Zhao, T. Guo, X. Li, T. Xu, B. Yang, X. Zhao, *Appl. Catal. B Environ.* **2018**, *224*, 725–732.

[37] L. Wang, B. Li, D. D. Dionysiou, B. Chen, J. Yang, J. Li, *Environ. Sci. Technol.* **2022**, *56*, 3386–3396.

[38] L. Li, L. Xu, Z. Hu, J. C. Yu, *Adv. Funct. Mater.* **2021**, *31*, 2106120.

[39] Y. Isaka, Y. Kawase, Y. Kuwahara, K. Mori, H. Yamashita, *Angew. Chem. Int. Ed.* **2019**, *58*, 5402–5406.

[40] C. Wu, Z. Teng, C. Yang, F. Chen, H. Bin Yang, L. Wang, H. Xu, B. Liu, G. Zheng, Q. Han, *Adv. Mater.* **2022**, *34*, 2110266.

[41] A. de Oliveira, G. F. de Lima, H. A. De Abreu, *Chem. Phys. Lett.* **2018**, *691*, 283–290.

[42] J. Qi, X. Yang, P. Y. Pan, T. Huang, X. Yang, C. C. Wang, W. Liu, *Environ. Sci. Technol.* **2022**, *56*, 5200–5212.

10.1002/anie.202309480

WILEY-VCH

RESEARCH ARTICLE

## Entry for the Table of Contents

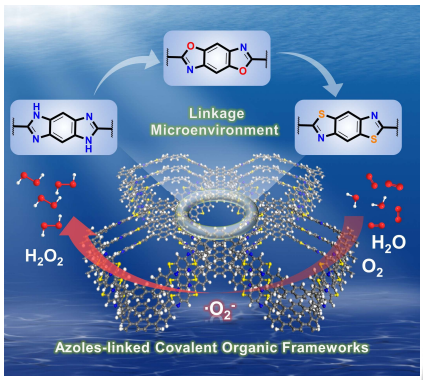


A tunable covalent organic framework (COF) platform with three azole-related linkages was prepared through linker exchange reactions. The linkage microenvironment changes the photoelectric properties and photocatalytic performance. The thiazole linkage was more favorable for the formation of $^*O_2$ intermediate in $H_2O_2$ production than that of the oxazole and imidazole linkages.